

# Strain Effects in large-scale atomistic quantum dot simulations

Fabiano Oyafuso<sup>\*1</sup>, Gerhard Klimeck<sup>1</sup>, Paul von Allmen<sup>1</sup>, Tim Boykin<sup>2</sup>, and  
R. Chris Bowen<sup>1</sup>

<sup>1</sup> Jet Propulsion Laboratory, 4800 Oak Grove Dr. MS 169-315, Pasadena, CA, 91109, USA

<sup>2</sup> Department of Electrical and Computer Engineering, University of Alabama in Huntsville, Huntsville, Alabama, 35899, USA

PACS 73.21.La

Atomistic computations of electronic properties for nanostructures with strain (such as self-assembled quantum dots) typically consist of two components – a calculation of the individual atomic positions and the eigenstates of interest in the resulting Hamiltonian. Such simulations ultimately require artificial boundary conditions either through a truncation of the simulation domain or by the imposition of periodic boundary conditions, which necessarily introduce inaccuracies in both components of the computation. In simulations that include up to about 20 million atoms, it is demonstrated that the simulation domain truncation has little impact on the direct computation of the electronic energies but causes considerable inaccuracies in the calculation of the atomic positions unless the simulation domain is made much larger than the central quantum dot structure. The long-range nature of the lattice distortions induced by lattice mismatch is consequently expected to significantly alter the electronic structure of nearby quantum dots.

## 1. Introduction

As the minimum feature size of nanostructures is reduced to the length of a few monolayers, the envelope function approximation, which is central to the **k.p** method commonly used to compute the electronic structure of quantum dots, becomes much less reliable [1]. Empirical tight-binding and pseudopotential methods are two alternative approaches that are used to model solids on these finer length scales. We have pursued the tight-binding approach for which accurate determinations of the relevant parameters have been available and improved upon over the past decades. We will thereby also benefit from our previous developments in Nanoelectronic Modeling (NEMO) [2,3,4]. Yet, even with empirical methods the ability to resolve variations on an atomic scale comes with a significant increase in computational expense. A typical self-assembled quantum dot contains “only” a few hundred thousand atoms, which constitutes a midsize problem by present day computational standards. However, in embedded quantum dots, it is insufficient to consider the quantum dot alone; the surrounding buffer material must be included as well. The total number of atoms that need to be included within the simulation domain to achieve convergence may then be two orders of magnitude larger. There are two distinct components in an atomistic calculation that includes strain effects – 1) the calculation of the individual atomic positions, and 2) the diagonalization of the resulting Hamiltonian operator for the eigenstates of interest. Because of the large computational expense associated with such simulations, it is particularly important to identify which component of the calculation contributes most to the convergence of the solution. In this paper, we discuss how the size of the buffer impacts the computation of the ground state eigenvalues, and identify the slow convergence of this calculation with respect to the problem size as being nearly entirely attributable to the slow convergence of the strain component of the calculation.

## 2. Model

Atomistic schemes such as tight-binding offer the potential for more accurate modeling, but one must include enough orbitals in the basis set and have a sufficiently large number of parameters (see Tables in

\* Corresponding author: fabiano@jpl.nasa.gov Phone: 818.393.2537, Fax: 818.393.4802

the Appendix) to describe their coupling as a function of bond length and bond angle in such a way that the bulk properties of a material can be reproduced under arbitrary strain conditions. Our tight-binding simulation employs a 20 orbital basis consisting of  $s$ ,  $p$ , and  $d$  orbitals as well as an excited  $s^*$  orbital, which has been shown to accurately reproduce the bulk properties of InAs and GaAs under the sort of hydrostatic and biaxial strains typically found in  $\text{In}_x\text{Ga}_{1-x}\text{As}$  quantum dots [5]. Our model uses a power-law generalization of Harrison's  $d^{-2}$  [6] scaling law to account for changes from ideal bond length between an anion-cation pair. The scaling exponents ( $\eta$  in Table 2) are different for each pair of orbital coupling but are typically on the order of 2. Because the basis functions used are orthogonalized Lowdin orbitals and not true atomic orbitals, diagonal (self-coupling) elements also obey a power-law scaling that is dependent on the location of the nearest neighbors ( $C$  in Table 2). A genetic algorithm package is used to fit experimentally determined band edges and effective masses at key symmetry points in the Brillouin zone [7,8,9]. The strain scaling parameters are optimized by fitting to results obtained from a pseudopotential calculation by Van de Walle [10]. The complete tight-binding parameterization is listed in Tables 1 and 2 in the appendix. The corresponding material properties such as band edges and effective masses are listed in Table 3 for InAs (the unstrained bulk material properties for GaAs are the same as listed in reference [7]). Table 3 shows that the associated InAs and InGaAs material properties that immediately affect the electronic structure in electronic devices deviate from known reference values by only a few percent. Only the heavy hole masses of InAs appear not to be very well matched with deviations of 10-20%. The atomic positions are computed using a valence force model (VFF), in which the crystal total strain energy, expressed as a sum over all nearest-neighbor bonds of a local strain energy [11, 12] is minimized.

### 3. Simulation Results

For all simulations in this work, the model structure is a single dome-shaped  $\text{In}_x\text{Ga}_{1-x}\text{As}$  quantum dot of diameter 30 nm and height 5.4 nm embedded in a finite GaAs box, which is intended to approximate an infinite domain of GaAs. Two different compositions of In are considered:  $x=1.0$  (pure InAs) and  $x=0.6$ . The quantum dot itself contains roughly  $1.2 \times 10^5$  atoms. We choose free boundary conditions that allow for the structure to expand without any external constraints. Such boundary conditions have been shown to yield eigenenergies that are similar to those obtained using periodic boundary conditions [13].

The fundamental question we attempt to answer is how large a domain must be modeled in order to accurately reproduce the electronic structure of a typical quantum dot in isolation. Fig. 1 shows the computed ground state electron and hole eigenenergies of the  $\text{In}_{0.6}\text{Ga}_{0.4}\text{As}$  and InAs QDs described above as functions of the thickness of the surrounding GaAs medium. The horizontal and relative vertical scales are identical in each of the subfigures, and the bulk GaAs valence band edge is chosen as the origin for the energy scale. Because of memory constraints\*\*, the electronic calculation is limited to a buffer size of 20 nm, which corresponds to a simulation domain consisting of roughly 9 million atoms. Since no external constraints are imposed on the system, the overall strain within the QD is underestimated from what it would be for an infinitely large buffer. Since the shift in the conduction band edge at  $\Gamma$  is positive for compressive hydrostatic strain [14], the electron eigenenergy monotonically increases as the buffer thickness increases and the underestimation of strain is reduced. We observe that for both QDs the electron or hole eigenenergies have converged to asymptotic values within a few meV and that the alloyed QD simulations approach convergence more rapidly. The differences in computed eigenvalues between the 16 and 20 nm buffer simulations are 5.5 meV (HH) and 12.2 meV (EL) for the InAs QD. These values are approximately halved for the alloyed QD. The faster convergence for the alloyed dot is due to the reduction in strain associated with a quantum dot whose average lattice constant more closely matches that of the surrounding medium. These results show that although the number of atoms contained within

\*\* Simulation was performed on a Beowulf cluster of 32 nodes. Each node contained two 800 MHz processors and 2GB of RAM. See discussion in reference [7].

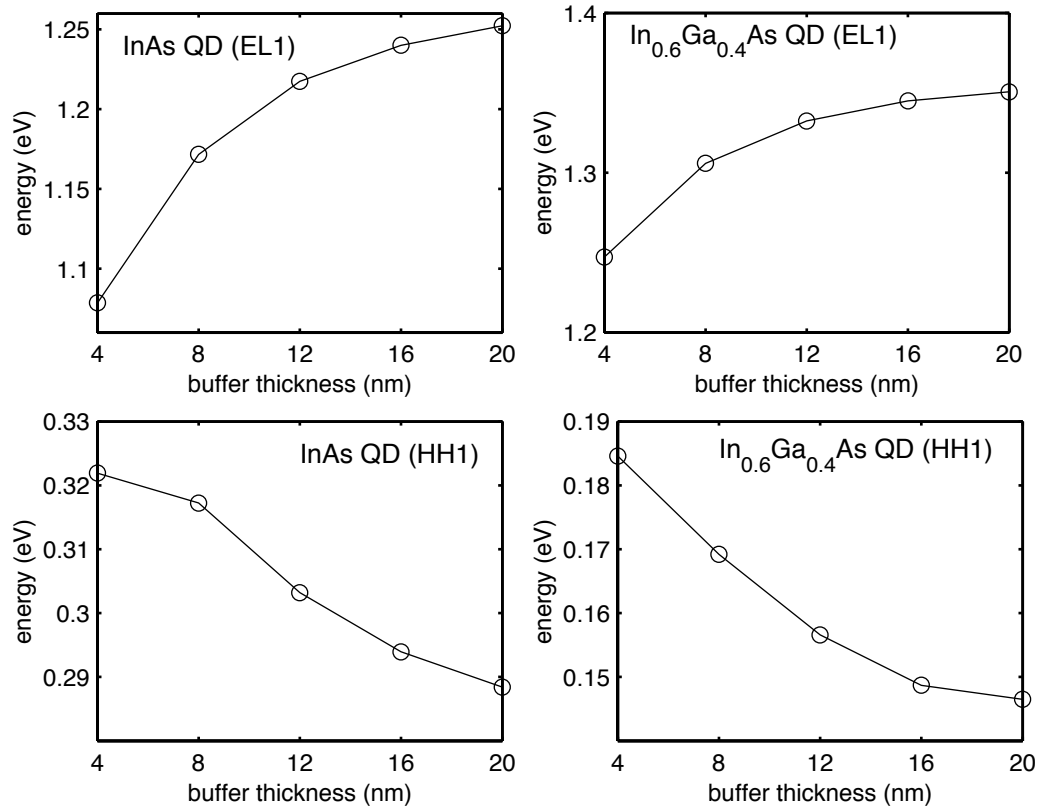


**Fig 1:** Ground state electron (EL) and heavy hole (HH) eigenenergies as a function of surrounding GaAs buffer size for dome-shaped InAs and In<sub>0.6</sub>Ga<sub>0.4</sub>As quantum dots.

a QD may "only" be on the order of  $10^5$ , the number of atoms that must be included in the simulation may be two orders of magnitude greater ( $\sim 9 \cdot 10^6$  for the 20nm buffer).

The size of the buffer needed for the eigenvalues to approximate those of an infinite buffer to within a particular tolerance depends on two effects -- the convergence of the strain calculation with buffer size and the convergence of the electronic solution. We shall demonstrate that the convergence of the strain calculation is the principal limiting factor in the overall precision of the electronic solution. We define "local" electron and hole eigenenergies as follows -- for each cation we compute the band minimum at  $\Gamma$  for a bulk crystal constructed from the single primitive cell formed by the cation and its four neighboring As anions. These eigenenergies depend only on the relative positions of a cation's neighbors and are therefore a direct reflection of the local strain conditions. Fig. 2 shows electron and hole local eigenenergies for the InAs QDs with 4nm and 24nm buffers<sup>††</sup> along two lines of cations. One line (along x) passes through the center of the dot and runs parallel to its base at a height equal to half the height of the dome; the other line (along z) passes through the major symmetry axis of the QD normal to its base. Only the  $\Gamma_6$  conduction band and  $\Gamma_8$  valence band, which is split into heavy and light hole states, are shown. Clearly, the local electronic states are very poorly represented by the small buffer calculation, differing from the 24 nm buffer calculation by up to 200 meV.

<sup>††</sup> Note: Although the electronic calculation limits the maximum problem size on our cluster computer to 20 nm, the strain component of the computation has less stringent memory requirements so that much larger buffers can be modelled. We intend to model even larger systems in the future.

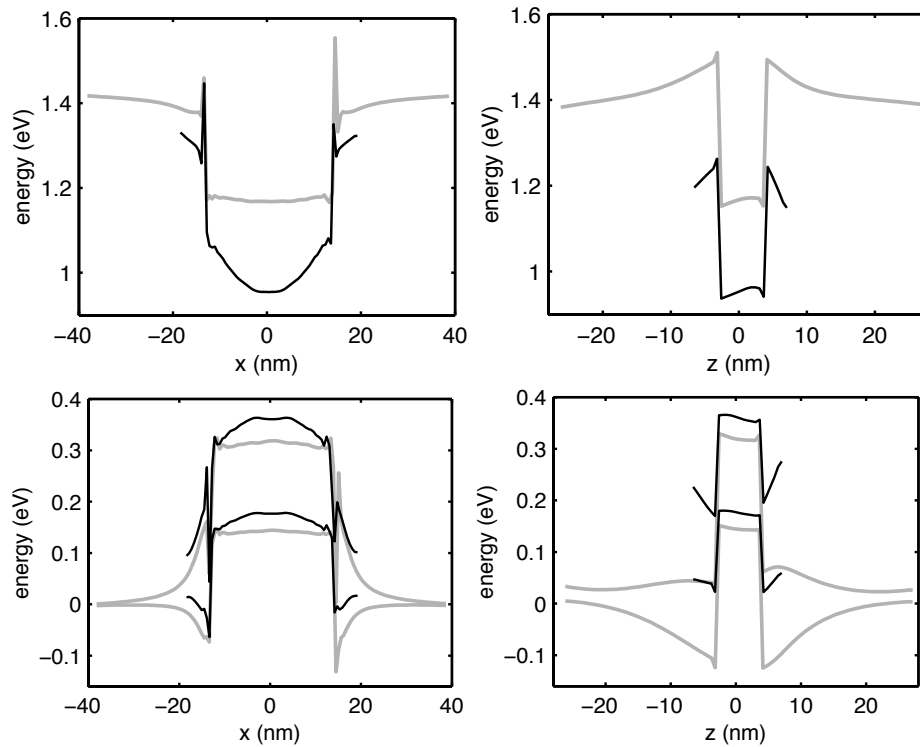


**Fig 2:** Electron (top) and hole (bottom) local eigenenergies in the  $x$  (left) and  $z$  (right) directions for 4nm (black) and 24 nm (grey) buffers for an InAs dome-shaped QD.

The plot along the  $z$  direction reveals that for the small buffer case, the local electronic eigenenergies just above and below the QD are lower than the asymptotic bulk value of 1.424 eV. This result indicates that the GaAs cells suffer a net tensile hydrostatic component of the strain as the GaAs cells stretch in the lateral direction to match the larger InAs lattice constant. For the large buffer, by contrast, the local electronic eigenenergies within the large buffer exceed the bulk value, which indicates a net compressive strain despite having to match the larger lattice constant of the compressed InAs within the QD. The reason for this result is that the cells above and below the dot cannot be arbitrarily displaced by the larger lattice constants in the QD, since they must ultimately match with GaAs cells on the lateral boundary of the simulation domain. The constraint imposed by the cells on the lateral faces of the boundary favors a slight vertical expansion of cells within the dot (relative to the GaAs lattice constant) at the expense of a net compression along  $z$  of the GaAs cells above and below the QD. The heavy-hole and light hole states on the other hand are less affected by the change in strain in the two cases, because the valence band deformation potentials for both GaAs and InAs are much smaller than those of the conduction band [15].

Fig. 3 shows plots the similar to Fig. 2 but for the alloyed  $\text{In}_{0.6}\text{Ga}_{0.4}\text{As}$  QD. Because of the alloying, the local eigenenergies do not form a continuous curve within the QD, but rather a discontinuous set of points due to a bi-modal distribution of In-As and Ga-As bondlengths [7]. From the plot of the electron eigenenergies along the  $x$  direction, one can discern two clusters of points separated by a gap ranging from about 1.2 eV to 1.3 eV. Points above (below) this gap correspond to Ga (In)-centered primitive cells. Of particular note in each subfigure is that the separation in energies within the GaAs buffer between the large and small buffers is much less than observed in Fig. 2. The large strain induced splitting

of the valence bands along the  $z$ -axis even at a buffer length of 24 nm of Fig. 2 is almost relaxed in Fig. 3. This is a direct consequence of reduced strain within the system.

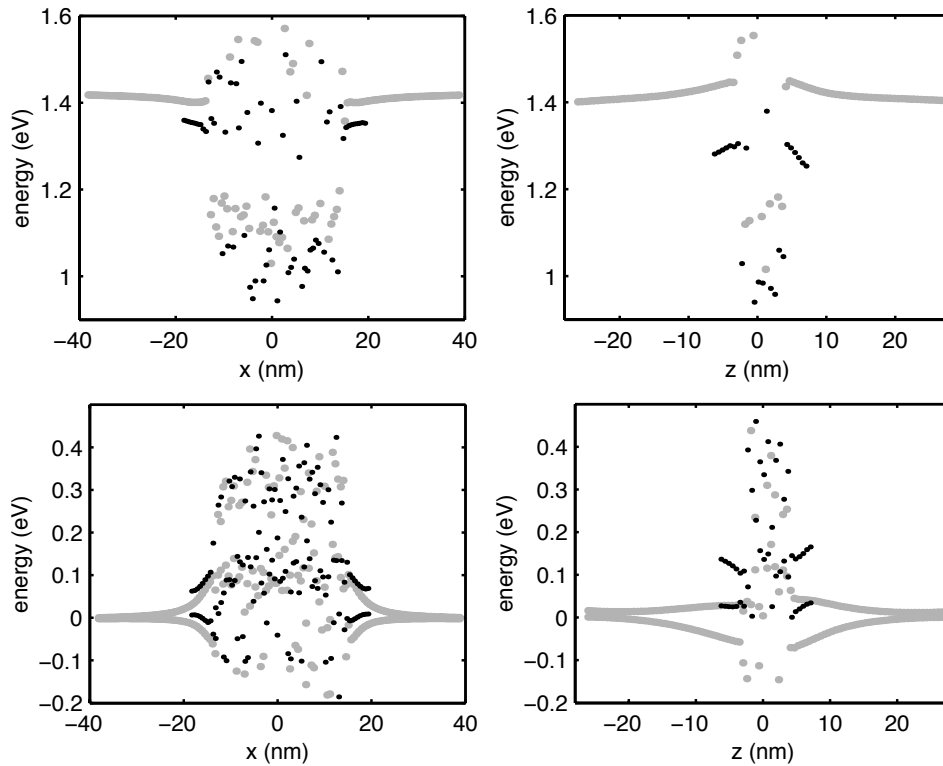


**Fig 3:** Electron (top) and hole (bottom) local eigenenergies in the  $x$  (left) and  $z$  (right) directions for 4 nm (black) and 24 nm (grey) buffers for an  $\text{In}_{0.6}\text{Ga}_{0.4}\text{As}$  dome-shaped QD.

Whilst the full electronic computation is limited to a buffer size of 20 nm because of memory constraints, computation of the minimum local eigenvalue (i.e. band edge) requires that only a strain calculation be performed so that larger buffer sizes can be explored. Since Fig. 2 shows that apart from a constant shift the spatial profile of the local eigenvalues along ( $z$ ) is roughly the same regardless of buffer size, the separation between computed eigenvalue and bandedge should be fairly constant, so that convergence of the bandedge energy should mirror convergence of the actual eigenvalue. Fig. 4 plots the minimum local eigenvalue (i.e. bandedge) together with the computed ground state energy for InAs. The separation between these two curves is indeed found to be fairly constant, differing by a maximum of 30 meV for the electron states and 9 meV for the hole states. The difference between the 20 nm and 24 nm bandedge is about 6 meV for the conduction band and 0.2 meV for the valence band.

Figs. 2 and 3 indicate the long-range effects of strain on the local bandstructure. Fig. 4 clearly shows the relation of the local bandstructure energy to the energy of the quantum confined ground states and their strong dependence on GaAs buffer. It is interesting to point out the physical difference in the extent and local atomic dependence of these different states. The local bandstructure depends solely on the immediate atomic neighbors only. The quantum dot ground states are extended over the central  $\text{In}_x\text{Ga}_{1-x}\text{As}$  quantum dot region, yet they are localized with respect to the surrounding GaAs buffer. The GaAs buffer provides the confinement potential to the extended  $\text{In}_x\text{Ga}_{1-x}\text{As}$  quantum dot states of interest. A very important issue to raise is the role of the proximity of an infinite wall confinement potential at the

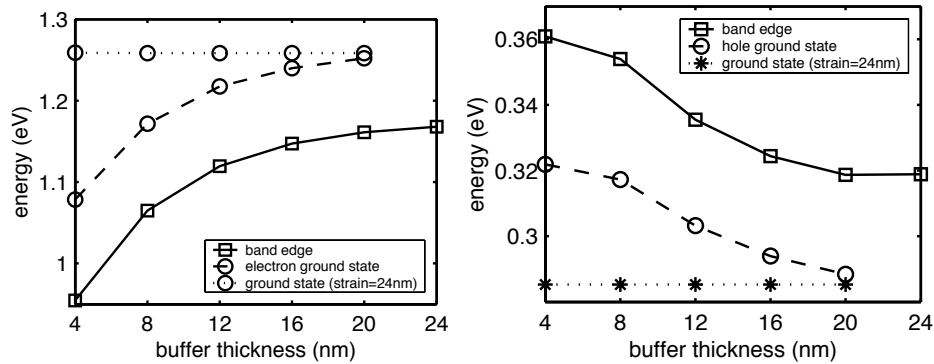


**Fig 4:** Ground state electron and hole eigenenergies (solid) and minimum band edge (dashed) in the InAs QD system. The dotted curve corresponds to eigenenergies computed using atomic positions determined from a strain calculation with a buffer size of 24 nm encompassing roughly 20 million atoms.

finite simulation domain. To address that issue the following numerical experiment was performed: The atomic positions were computed for a buffer size of 24nm and the electron and hole ground states were computed for different electronic hard wall buffer sizes assuming the atomic positions computed for the 24nm buffer size. The results are shown as dotted lines in Fig. 4. The ground state energies are essentially constant for buffer sizes greater than 4 nm varying by a maximum of 0.4 meV. In fact, even a buffer of about 1 nm (2 monolayers, not shown in Fig. 4) yields eigenvalues that differ from the infinite buffer result by only 8 meV. This can be interpreted such that the extended quantum dot wavefunctions in the  $\text{In}_x\text{Ga}_{1-x}\text{As}$  quantum dots penetrate into the surrounding buffer layer only a few monolayers deep and the corresponding eigenstates is very weakly dependent on the proximity of the electronic hard wall boundary condition in the GaAs buffer.

These results prove that the accuracy of our simulation is limited entirely by the slow asymptotic convergence of the computation of atomic positions, and not by the electronic portion of the computation. An important consequence of this result and a central result of this work is that two quantum dots which are separated sufficiently far away that they may be considered electronically uncoupled can still significantly alter each other's electronic eigenstates through long-range lattice distortions.

#### 4. Conclusions

We have presented a tight-binding-based calculation of electronic states within a quantum dot and analysed its dependence on the size of the simulation domain. It was found that convergence toward the asymptotic solution of an infinite buffer is quite slow with increasing buffer size. The long-range influence of distortions of the lattice on the electronic structure is identified as the principal cause of this slow convergence, whereas truncation of the electronic structure simulation domain has relatively very little impact on the computed eigenvalues. The impact of this result is that quantum dots, which are electronically uncoupled, may still have a strong influence on each other from the long range of the strain field.

**Acknowledgements** The work described in this publication was carried out at the Jet Propulsion Laboratory, California Institute of Technology. The Beowulf cluster on which our calculations were performed was provided by funding from the NASA Offices of Earth Science, Aeronautics, and Space Science and the Center for Integrated Space Microsystems. This work was funded by grants from NSA/ARDA (quantum computing), ONR (nanoelectronic modeling), and JPL internal Research and Development (evolvable computation and spintronics). The authors would like to thank Akos J. Czikmantory for his work on the NEMO 3-D graphical user interface, Dr. E. Robert Tisdale for his work on independent, license free math libraries, Hook Hua for his integration of various new math

and I/O libraries into NEMO 3-D, and J. Zachary Isaacs and Nooshin Meshkaty for their maintenance of the Beowulf cluster.

## References

- [1] T.G. Dargam, R.B. Capaz, and B. Koiller, Phys. Rev. B, **56** p.9625, (1997)
- [2] R.C. Bowen, W.R. Frensley, G. Klimeck, and R. Lake, Phys. Rev. B, **52**, p.2754 (1995)
- [3] G. Klimeck, R. Lake, R.C. Bowen, W. Frensley, and T. Moise, Appl. Phys. Lett., **67**, p.2539 (1995)
- [4] R.C. Bowen, G. Klimeck, R. Lake, W.R. Frensley, and T. Moise, J. Appl. Phys., **81**, p3207 (1997)
- [5] T. Boykin, G. Klimeck, R.C. Bowen, F. Oyafuso, Phys. Rev. B, **66**, 125207 (2002)
- [6] W. Harrison, *Elementary Electronic Structure*, (World Scientific, New Jersey, 1999)
- [7] G. Klimeck, et al., Computer Modeling in Engineering Science, **3**, 601 (2002) .
- [8] G. Klimeck, R.C.~Bowen, and T. Boykin, Phys. Rev. B, **63**, 195310 (2001)
- [9] G. Klimeck, R.C.~Bowen, and T. Boykin, T. Cwik, Superlatt. and Microstruct., **27**, 519 (2000)
- [10] C. Van de Walle, Phys. Rev. B., **39**, 1871 (1989)
- [11] P. Keating, Phys. Rev., **145**, 637 (1966)
- [12] C. Pryor, J. Kim, L.W. Wang, A.J. Williamson, and A. Zunger, J. of Appl. Phys., **83**, 2548 (1998)
- [13] F. Oyafuso et al, accepted for publication in Physica Status Solidi, (2003)
- [14] P. Bhattacharya, *Properties of Lattice-Matched and Strained Indium Gallium Arsenide*, vol. 8, INSPEC, London, (1993)
- [15] R. Weihofen, G. Weiser, C.H. Starck, R.J.Simes, Phys. Rev. B, **51**, 4296 (1995)





## Appendix

Table 1 lists the  $sp^3d^5s^*$  tight binding model parameters needed for the construction of the unstrained Hamiltonian. Table 2 lists the strain scaling parameters corresponding to the model presented in detail in references [5,7]. Table 3 presents the unstrained bulk material parameters for InAs and  $In_{0.5}Ga_{0.5}As$ . In this work we have improved the behavior of InAs subject to hydrostatic strain compared to reference [7] by fitting the In-As coupling matrix elements, the In on-site elements together with the strain parameters  $\eta$  and  $C$ . The alloy  $In_{0.5}Ga_{0.5}As$  is included in the optimization process within the limits of a virtual crystal approximation in order to guarantee proper alloy mixing behavior. We have found in the past that excellent binary component fits to GaAs and InAs alone may still result in a bad parameterization for the InGaAs alloy in the VCA as well as random distribution approach. It is pointed out here explicitly that the VCA approach is only used in the parameterization and that the full 3-D simulations do not make use of that assumption, resulting in noisy local potentials as described in Figure 3.

**Table 1** InAs/GaAs tight-binding parameters in  $sp^3d^5s^*$  model. All units are in eV except for lattice constant in Angstroms.

Parameter	GaAs	InAs
$E_{sa}$	-5.50042	-5.50042
$E_{pa}$	4.15107	4.15107
$E_{sc}$	-0.24119	-0.53824
$E_{pc}$	6.700776	7.76234
$E_{s^*a}$	19.71059	19.71059
$E_{s^*c}$	22.66352	18.76447
$E_{da}$	13.03169	13.03169
$E_{dc}$	12.74846	13.44722
$\lambda_a$	0.17234	0.17234
$\lambda_c$	0.02179	0.13967
$ss\sigma$	-1.64508	-1.53021
$s^*s^*\sigma$	-3.67720	-3.99086
$s_a^*s_c\sigma$	-2.20777	-2.31717
$s_as_c^*\sigma$	-1.31491	-1.36162
$s_ap_c\sigma$	2.66493	3.18532
$s_cp_a\sigma$	2.96032	2.37527
$s_a^*p_c\sigma$	1.97650	2.34216
$s_c^*p_a\sigma$	1.02755	0.60111
$s_ad_c\sigma$	-2.58357	-2.27077
$s_cd_a\sigma$	-2.32059	-1.87451
$s_a^*d_c\sigma$	-0.62820	-0.67754
$s_c^*d_a\sigma$	0.13324	-0.21773
$pp\sigma$	4.15080	4.49803
$pp\pi$	-1.42744	-1.41734
$p_ad_c\sigma$	-1.87428	-1.80534
$p_cd_a\sigma$	-1.88964	-2.12734
$p_ad_c\pi$	2.52926	2.43089
$p_cd_a\pi$	2.54913	2.52183
$dd\sigma$	-1.26996	-1.34592
$dd\pi$	2.50536	2.67210
$dd\delta$	-0.85174	-0.45412
$a$	0.565320	0.60583
$E_{shift}$	27.00000	27.00000

**Table 2** InAs/GaAs tight-binding dimensionless scaling exponents and diagonal parameter shift constants defined in Ref [5,7].

Parameter	GaAs	InAs
$\eta_{s,s^*\sigma}$	0.00000	0.00000
$\eta_{s^*,s^*\sigma}$	0.21266	0.34902
$\eta_{s,s\sigma}$	2.06001	1.87635
$\eta_{s,p\sigma}$	1.38498	1.25042
$\eta_{p,p\sigma}$	2.68497	2.73407
$\eta_{p,p\pi}$	1.31405	1.32992
$\eta_{s,d\sigma}$	1.89889	1.65530
$\eta_{s^*,p}$	1.39930	1.11454
$\eta_{p,d\sigma}$	1.81235	2.32014
$\eta_{p,d\pi}$	2.37964	2.57895
$\eta_{d,d\sigma}$	1.72443	2.00323
$\eta_{d,d\pi}$	1.97253	1.84572
$\eta_{d,d\delta}$	1.89672	2.07788
$\eta_{s^*,d\sigma}$	1.78540	3.00000
$C_{s,s}$	0.58696	0.25331
$C_{s^*,s^*}$	0.48609	0.00000
$C_{s^*,d,sc}$	0.88921	2.97410
$C_{sa,s^*c}$	0.77095	2.99811
$C_{sa,pc}$	0.75979	0.93102
$C_{sc,pa}$	1.45891	3.00000
$C_{s^*,a,pc}$	0.81079	0.00000
$C_{s^*,c,pa}$	1.21202	2.24414
$C_{sa,dc}$	1.07015	0.00001
$C_{sc,da}$	0.38053	3.00000
$C_{s^*,a,dc}$	1.03256	0.00000
$C_{s^*,c,da}$	1.31726	0.00000
$C_{p,p}$	0.00000	2.36738
$C_{pa,dc}$	1.61350	0.15676
$C_{pc,da}$	0.00000	0.49725
$C_{d,d}$	1.26262	0.16244

1

**Table 3** Experimentally available InAs and  $\text{In}_{0.5}\text{Ga}_{0.5}\text{As}$  properties derived from tight-binding parameters in Table 1 with values targeted by the genetic algorithm.

InAs Parameter	Value	Target	Rel. Error (%)
$E_g(\Gamma)$	0.3705397	0.37000	0.15
$E_c(\Gamma)$	0.5908215	0.59570	0.82
$V_{hh}$	0.2202818	0.22570	0.54
$\Delta_{so}$	0.4024390	0.38000	5.90
$m_e^*[001]$	0.0232215	0.02390	2.84
$m_{lh}^*[001]$	-0.0274066	-0.02730	0.39
$m_{lh}^*[011]$	-0.0265158	-0.02640	0.44
$m_{lh}^*[111]$	-0.0262440	-0.02610	0.55
$m_{hh}^*[001]$	-0.3105819	-0.34480	9.92
$m_{hh}^*[011]$	-0.5015785	-0.63910	21.52
$m_{hh}^*[111]$	-0.6237285	-0.87640	28.83
$E_c(X) - E_c(\Gamma)$	1.8610995	1.91000	2.56
$k_X$	0.9950000	0.90000	10.56
$E_c(L) - E_c(\Gamma)$	1.1631529	1.16000	0.27
$k_L$	1.0000000	1.00000	0.00
$E(\Gamma_{6v})$	-12.9315017	-12.30000	5.13
$E(\Gamma_{6c})$	0.3705397	0.37000	0.14
$E(\Gamma_{7c})$	3.6640374	4.39000	16.54
$E(\Gamma_{8c})$	3.9591610	4.63000	14.49
$E(X_{6v})$	-2.4442016	-2.40000	1.84
$E(X_{7v})$	-2.3445616	-2.40000	2.31
$E(X_{7c})$	2.8460917	2.50000	13.84
$E(L_{4v})$	-10.8116909	-10.92000	0.99
$E(L_{5v})$	-5.3983166	-6.23000	13.35
$E(L_{6v})$	-1.3684759	-1.20000	14.04
$E(L_{7v})$	-1.0710516	-0.90000	19.01
$E(L_{6c})$	1.5336926	1.50000	2.25
$E(L_{7c})$	4.2050934	5.40000	22.13
InGaAs	Value	Target	Rel. Error (%)
$E_g(\Gamma)$	0.8933567	0.897000	0.41
$E_c(\Gamma)$	1.0083650	1.009850	0.15
$V_{hh}$	0.1150083	0.112850	1.91
$V_{lh}$	0.1150083	0.112850	1.91
$V_{so}$	-0.2486715	-0.247150	0.62

2

3

4

5

6